A study of cross-shore maximum upwelling intensity along the Northwest Africa coast

Zhaoyun Chen, Xiao-Hai Yan, Yuwu Jiang, Lide Jiang & Young-Heon Jo

Journal of Oceanography
edited by The Oceanographic Society of Japan

ISSN 0916-8370

J Oceanogr
DOI 10.1007/s10872-013-0185-5

Springer

J Oceanogr
DOI 10.1007/s10872-013-0185-5

ORIGINAL ARTICLE

A study of cross-shore maximum upwelling intensity along the Northwest Africa coast

Zhaoyun Chen · Xiao-Hai Yan · Yuwu Jiang · Lide Jiang · Young-Heon Jo

Received: 15 October 2012 / Revised: 5 May 2013 / Accepted: 31 May 2013

Abstract Satellite images of sea surface temperature (SST) show that the location of cross-shore SST minimum (LCSM) stretches along the isobaths in the Northwest Africa Upwelling System. To understand and interpret these observations better, we set up a two-dimensional analytical model that takes into account the surface and bottom Ekman transport and the alongshore geostrophic current, as well as bottom friction and variations in bottom topography. The structure of vertical velocity with a realistic topography clearly illustrates the variations of SST drop in a sample cross-shore section. Some idealized theoretical model experiments are carried out to examine the effects of eddy viscosity, Coriolis force, and cross-shore wind on the location of the cross-shore maximum upwelling intensity. The results show that the cross-shore wind largely impacts on the location where the coldest water outcrops to the surface through an adjustment of the cross-shore pressure gradient. This is also verified by the remotely sensed data, which indicate that the maximum correlation coefficient between cross-shore wind stress and the depth of LCSM is −0.65 with a lag of approximately 1 day.

Keywords Northwest Africa upwelling · Sea surface temperature · Minimum SST · Analytical model · Cross-shore wind

1 Introduction

The Northwest Africa Upwelling System (NAUS) off the northwest coast of Africa is chosen to study the cross-shore minimum sea surface temperature (SST) along the coast due to its wide shelf and strong upwelling. It is one of the four main eastern boundary current upwelling systems in the world and usually extends to several hundred kilometers offshore (Arístegui et al. 2009). The northeast trade wind is the predominant wind feature in the NAUS area (Johnson and Stevens 2000), and the upwelling takes place throughout the year from 20°N to 33°N (Marcello et al. 2011). Estrade et al. (2008) found that the core of the upwelling off Northwest Africa was sometimes far away from the coast. They further concluded that the upwelling cell was essentially concentrated in the region where the water depth was between $0.5D$ and $1.25D$ (D is the thickness of the Ekman layer) using analytical and numerical models. Ryan et al. (2001) showed that the pigment-rich bands of surface chlorophyll coincided with the lowest surface temperature along the 60 and 100 m isobaths. Roy (1998) observed that SST was at its minimum over the shelf far away from the coast off South Senegal, and fish tended to spawn away from the main upwelling center areas dominated by strong wind mixing and offshore transport. The location of the cross-shore maximum upwelling along the coast, which is

Z. Chen · X.-H. Yan · Y. Jiang (✉)
State Key Laboratory of Marine Environmental Science, Xiamen University, Xiamen 361005, China
e-mail: ywjiang@xmu.edu.cn

Z. Chen · X.-H. Yan · Y.-H. Jo
Center for Remote Sensing, College of Earth, Ocean and Environment, University of Delaware, Newark, DE 19716, USA

L. Jiang
NOAA/NESDIS/STAR, E/RA3, NOAA Science Center, 5200 Auth Road, Camp Springs, MD 20746, USA

Published online: 25 June 2013

characterized by the minimum SST and high Chl-*a* concentration, may play a significant role in the hydrodynamic transport and the distribution of plankton and zooplankton.

In this study, we set up a two-dimensional analytical model (Kamenkovich 1977; Estrade et al. 2008) including the Ekman and geostrophic components to locate the corresponding depth of the cross-shore maximum upwelling. We find that it is closely related to eddy viscosity, Coriolis force, and cross-shore wind stress. We then offer an explanation for why the location of cross-shore SST minimum (LCSM) approximately aligns with the isobaths in the NAUS area as our results indicated.

2 Data and analytical solution

The Moderate Resolution Imaging Spectroradiometer (MODIS) SST data from OceanColor website (http://oceancolor.gsfc.nasa.gov/) are used to locate the LCSM along the coast off the NAUS area in 2008. The relevant wind stress (0.25° resolution) along the coast is obtained from the QuikSCAT satellite by the Jet Propulsion Laboratory. ETOPO1 (1°/60°) in the National Geophysical Data Center (USA) provides the topography for the study area.

The analytical model we used in this study is from Estrade et al. (2008). Ekman's solution is extended to include internal geostrophic currents in coastal areas with finite depth. More details on the derivation of horizontal velocity are given in the Appendix. The vertical velocity W can then be calculated from the cross-shore velocity U (real part of $\vec{V}$ in Eq. (10)) based on the continuity equation:

$$\frac{\partial U}{\partial x} + \frac{\partial W}{\partial z} = 0, \tag{1}$$

where x and z are in cross-shore and vertical directions. The analytical model is one-dimensional in the horizontal plane, and is two-dimensional in the vertical section according to Eq. (1). An eddy viscosity $A_z = 3.5 \times 10^{-3}$ m^2 s^{-1} is chosen to compute the velocity structures, which is almost constant within the bottom 7 m from the observations (Souza et al. 2004).

3 Results and discussion

The study domain in the NAUS area extends from (20.5°N, 18°W) to (25°N, 14.5°W). Figure 1a shows the SST data with 1 km resolution with some slight cloud cover. The continental shelf is dominated by the cool upwelling water off the coast. After filtering the SST image with a 3 × 3 averaging box filter to reduce the noise caused by clouds, the location of the LCSM along the coast can be determined (red line in Fig. 1c). North of 23°N, the LCSM extends along the 25 m isobath, whereas south of 23°N, it almost aligns with the 35 m isobath except the few data that appear at the shelf break. To explain the deeper corresponding depth from which the cold subsurface water outcrops to the surface south of 23°N, we examine the cross-shore wind stress (Fig. 2a) from wind control points (asterisks in Fig. 1a) along the coast. Note that the wind control points are set at a distance from the coastline of approximately 50 km to avoid the effects of coastal masking. North of 23°N, the cross-shore wind stress is less than 0.008 N m^{-2}, and increases to more than 0.02 N m^{-2} in the southern part. It appears that the onshore wind causes the LCSM to move offshore (further illustrated in the later part). From the continuity equation (1), one may doubt that the location of the maximum vertical velocity (i.e., LCSM presented in Fig. 1c) largely depends on the topography slope; however, when we check the cross-shore maximum topography gradient on the shelf (blue dots in Fig. 1c), we find that the LCSM seldom follows the location of the maximum gradient value. The same processes are executed in the monthly averaged SST and the corresponding cross-shore wind stress in June 2008 (Figs. 1b, d, 2b). They show very similar results to that of the analysis on 14 June 2008.

To explain these phenomena, an analytical model is used. The cross-shore velocity U can be computed according to Eq. (10), and vertical velocity W is derived on the basis of continuity equation (1). As an example, we take alongshore wind stress $\tau_y \approx 0.16$ N m^{-2} and cross-shore wind stress $\tau_x \approx 0$, with $f = 6 \times 10^{-5}$ s^{-1} at the cross-shore section off approximately 24°N (Fig. 1c). Figure 3a and b show the cross-shore velocity U and vertical velocity W with a constant bottom slope ($\alpha = 0.001$). The field of U shows that the Ekman effect dominates in the upper layer within a 20 m depth, and drives the currents offshore. In the bottom layer, the return current flows onshore and interacts with the surface Ekman offshore flow over the inner shelf of 60 km offshore. The inner shelf is defined as the transition region where surface and bottom Ekman layers interact with each other (Lentz 1995). The bottom onshore current uplifts along the shelf and upwells to the surface in coastal region (Fig. 3b). These dynamical forcings bring the cold deep water to the surface and yield an extensive upwelling region in the coastal area. Here, we average W from the surface to the Ekman depth. It has a maximum value at 22.7 km offshore, and gradually decreases to zero at 44 km offshore. The location of the SST minimum is then expected to occur near the 22.7 m isobath. This is very close to the observed result that the LCSM aligns with the 25 m isobath. The negative W outside the upwelling region means that there is a downwelling over the outer shelf. When we integrate offshore velocity from the surface to the

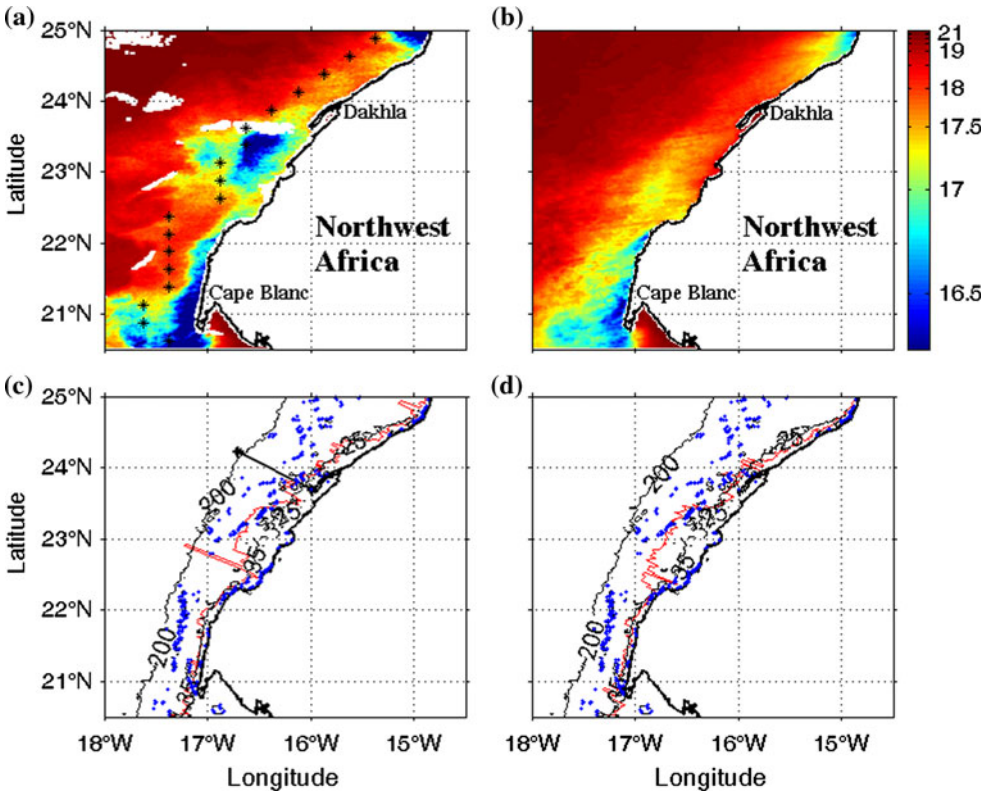

Fig. 1 **a** MODIS SST (°C) image on 14 June 2008 off the northwest coast of Africa. *Asterisks* along the coast mark the wind control points. **b** Monthly mean SST in June 2008. **c**, **d** The bathymetry (meters) off the northwest coast of Africa. Over the interior shelf, 25 m isobath is shown north of 23°N, and 35 m isobath is shown in the southern part. The *blue dots* represent the cross-shore maximum topography gradient over the shelf. *Red line* is the corresponding location of cross-shore SST minimum along the coast (*left panel* for **a** and *right panel* for **b**). *Line connecting asterisks* is a sample cross-shelf section perpendicular to the 25 m isobath

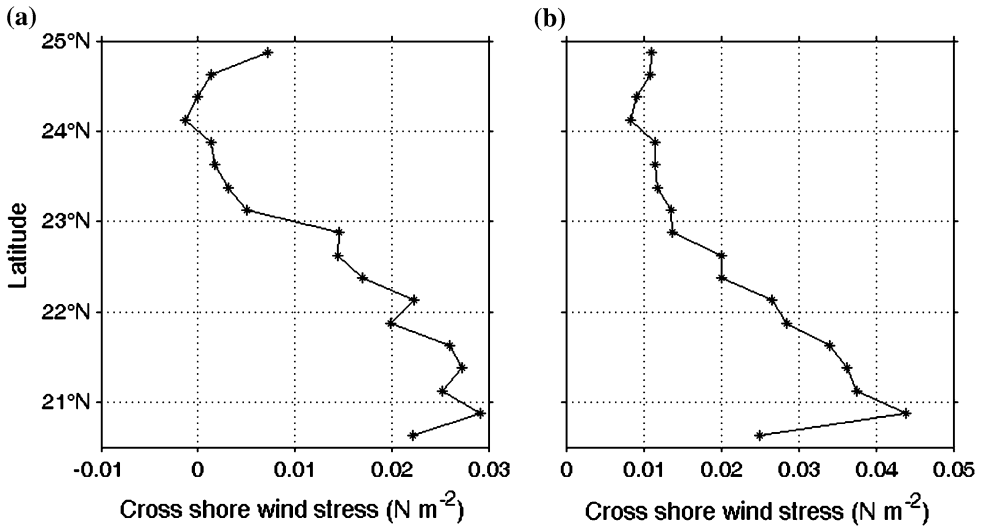

Fig. 2 **a** Cross-shore wind stress (N m^{-2}) on 14 June 2008 (positive eastward). **b** Monthly averaged cross-shore wind stress (N m^{-2}) in June 2008

first zero crossing of the flow as offshore Ekman transport, we find an overshoot at ~44 km offshore; then it gradually decreases to full Ekman transport in regions with depth deeper than 75 m (data not shown). This is consistent with numerical model result with exponential eddy viscosity profile by Lentz (1995). The convergence of the Ekman transport at 44–75 km offshore in the surface layer causes the downwelling process.

It is straightforward to apply the analytical model to a realistic topography. Thus, we take the sample cross-shore section in Fig. 1c. The topography is smoothed to remove the influence of the fluctuation of the topographic slope. The cross-shore velocity U and vertical velocity W are presented in Fig. 3c and d. The fields of U and W are similar to the constant slope case. The onshore return flow is narrow and exhibits large W at steep topography, whereas it is opposite in the case of gentle slope. The strong upwelling climbs over the shelf break and displays an upwelling core at 20 m depth.

We further average the W field in the Ekman layer as $\bar{W}$ and compare it to the SST drop, which can be seen as an

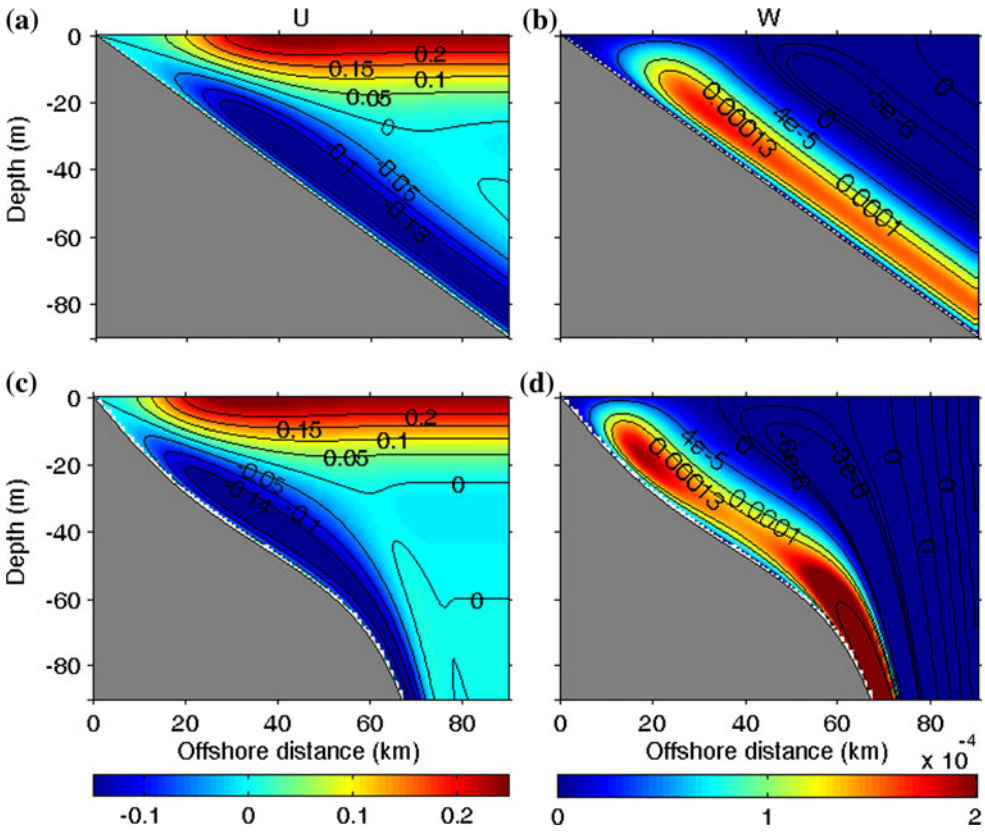

Fig. 3 **a**, **b** Cross-shore velocity U (m s^{-1}) and vertical velocity W (m s^{-1}) with an idealized shelf ($\alpha = 0.001$). **c**, **d** Cross-shore velocity U (m s^{-1}) and vertical velocity W (m s^{-1}) with a smoothed topography from the sample section in Fig. 1c

upwelling index, in the sample cross-shore section on 14 June 2008 (Fig. 4). SST drop is defined as the SST difference between oceanic (here we choose 21 °C) and coastal locations in each pixel (Wooster et al. 1976; Santos et al. 2005). The $\bar{W}$ firstly increases and shows a peak at 16 km offshore (corresponding depth is $\sim$23.6 m) which then decreases to zero at 36 km offshore. Alongside the upwelling is a downwelling area extending approximately 28 km wide. The SST drop reaches its maximum near the largest $\bar{W}$, and rapidly decreases in the downwelling area and the open ocean. The field of $\bar{W}$ favorably reproduces the hydrodynamic conditions in the sample cross-shore section, and explains the LCSM and the variations of ΔT.

To further analyze the factors influencing the LCSM, some idealized experiments are performed. The analytical model is run for different vertical eddy viscosities A_z with a constant bottom slope ($\alpha = 0.001$), constant Coriolis parameter, uniform alongshore wind stress, and no cross-shore wind. The corresponding depth of the maximum $\bar{W}$ in the Ekman layer is then plotted against the square root of different A_z (Fig. 5a), and a strictly linear relationship between them is noticed. The upwelling extends throughout a wide area and with a small magnitude for $\bar{W}$ when the eddy viscosity is large, causing the LCSM to move offshore. This is because the region where the divergence occurs depends on the extent of the momentum transfer

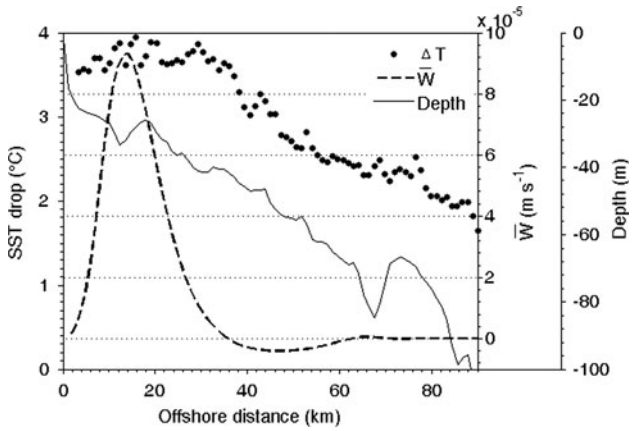

Fig. 4 SST drop (°C) along the sample section on 14 June 2008. $\bar{W}$ (*dashed line*) is the averaged vertical velocity (m s^{-1}) in the Ekman layer obtained from Fig. 3d

from the surface to the bottom. The extent of the momentum transfer is related to the eddy viscosity (Lentz 1995). Similarly, the responses to varying Coriolis parameters f are examined with a constant eddy viscosity and alongshore wind stress. Figure 5b shows that the depth of the cross-shore maximum upwelling is proportional to $1/\sqrt{f}$. It is not surprising, in this case, that smaller Coriolis force induces stronger offshore Ekman transport and a deeper Ekman layer, and thus results in a stronger and

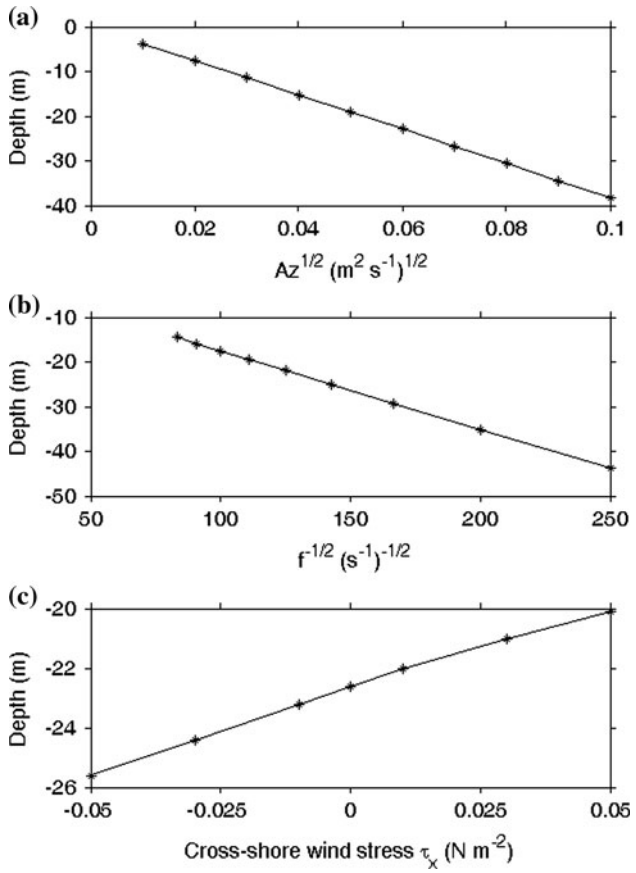

Fig. 5 Idealized experiments. The corresponding water depth of the maximum upwelling intensity with **a** different A_z ($f = 6 \times 10^{-5}$ s^{-1}, $\tau_x = 0$, $\tau_y = 0.05$ N m^{-2}); **b** different f ($A_z = 3.5 \times 10^{-3}$ m^2 s^{-1}, $\tau_x = 0$, $\tau_y = 0.05$ N m^{-2}); **c** different cross-shore wind stress ($f = 6 \times 10^{-5}$ s^{-1}, $A_z = 3.5 \times 10^{-3}$ m^2 s^{-1}, $\tau_y = 0.05$ N m^{-2})

wider upwelling region, and forces the LCSM to move further offshore. To explain the effect of onshore wind stress on the LCSM observed in Fig. 1, we perform the sensitivity experiments of cross-shore wind stress with $f = 6 \times 10^{-5}$ s^{-1}, a constant eddy viscosity, and uniform alongshore wind stress (Fig. 5c). The LCSM is further offshore when the cross-shore wind component is onshore than when the component is offshore, e.g., the difference can be 5.5 m when the onshore wind changes to offshore with the magnitude 0.05 N m^{-2}. This means the LCSM shifts a horizontal distance of 5.5 km over a wide continental shelf ($\alpha = 0.001$). The resulting cross-shore profile of vertical velocity W is shown in Fig. 6 in the cases of onshore and offshore wind component $\tau_x = \pm 0.05$ N m^{-2}. There are notable differences in the cross-shore current circulation response to onshore or offshore wind. The onshore wind drives a weak and small downwelling area in the near-shore part of the main upwelling region, and makes the LCSM offshore. This can be explained by the fact that the cross-shore wind component is the dominant effect in the pressure gradient adjustment in the shallow water ($h < 0.35D$), and the onshore wind component produces an opposite pressure gradient in the offshore direction and thus a downwelling area in the shallow water near the coast (Estrade et al. 2008). The onshore wind reduces the surface offshore velocity, and induces a thicker surface Ekman layer to ensure the full Ekman transport (data not shown). On the other hand, the offshore wind allows the upwelling process to extend into the shallower shelf. It is interesting to note that, when constant eddy viscosity is assumed, the alongshore wind stress does not change the LCSM, but the upwelling intensity instead. Actually, in a real ocean, because a greater wind stress implies a larger eddy viscosity, the LCSM will shift with different alongshore wind strengths.

The theoretical model experiments have shown the effect of cross-shore wind component on the LCSM. To further verify this effect, Fig. 7a depicts the time series of the depth of LCSM using 8-day averaged SST data (23–25°N, solid line) and the related cross-shore wind stress with 1 lag day (dashed line) in 2008. Before averaging the corresponding depth derived from the SST images, anomalies larger than two times the standard deviation are discarded. Note that the coastline orientation south of 23°N is rather changeable, and thus we only consider the region 23–25°N in the calculation. The cross-shore wind stress shows a sequence between −0.025 and 0.05 N m^{-2}. The offshore wind appears in winter, and the maximum onshore wind appears in summer. Accordingly, the depth of LCSM ranges from −33 to −20 m. It is apparent that the onshore wind is related to a deeper corresponding depth of LCSM and the offshore wind is related to a shallower corresponding depth of LCSM. The correlation coefficient between them is $r = -0.65$ ($p \approx 0$). It is also calculated by taking into account the different lag days (Fig. 7b). A positive value means that the response of the corresponding depth lags behind the wind, and a negative value indicates the other way around. The correlation coefficient firstly increases and then decreases as the lag day increases, and reaches its maximum value at 1 lag day. This implies that the atmospheric forcing on the ocean needs a response time to shift the LCSM. This is because when the wind changes, it takes time for the cold subsurface water to advect to the surface; thus, the location where the cold water outcrops may not change immediately. The variation of alongshore wind also influences the LCSM (Fig. 7c, $r = 0.46$, $p = 0.002$), but the effect is less important than the cross-shore wind, not only because of its smaller correlation, but also the need for stronger intensity in shifting the LCSM. The stronger alongshore wind seems to produce a deeper corresponding depth of LCSM, because the eddy viscosity is larger in the stronger wind condition. The correlation coefficient also shows a peak value at 1 lag day (Fig. 7d).

In our study area, the Coriolis parameter f can be treated as a constant. The estimated A_z is in the range of 10^{-3} to

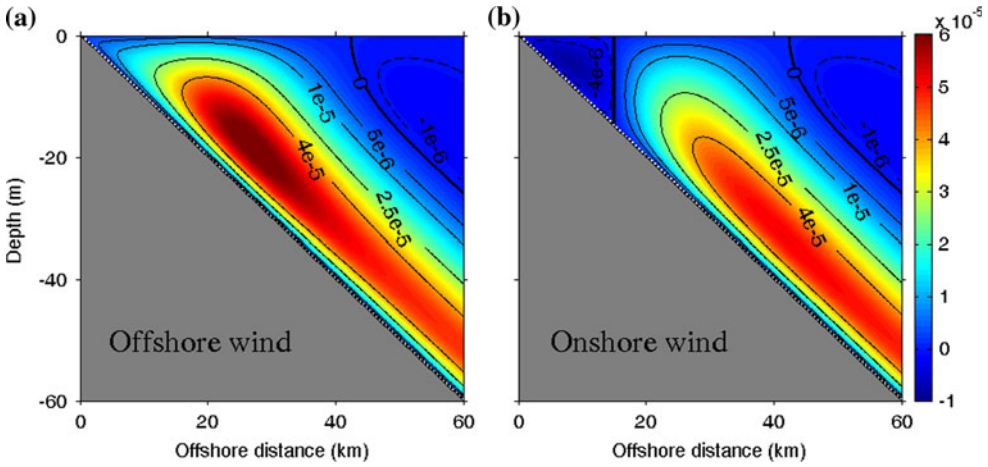

Fig. 6 Vertical velocity W (m s^{-1}) for **a** offshore wind stress $\tau_x = 0.05$ N m^{-2}; **b** onshore wind stress $\tau_x = -0.05$ N m^{-2}

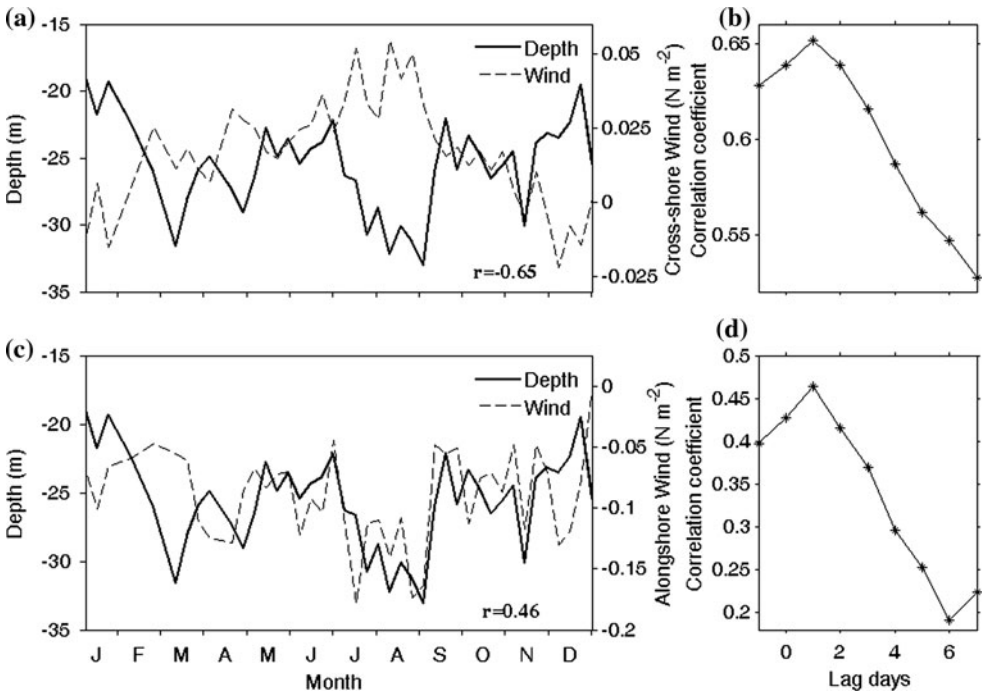

Fig. 7 Time series of the corresponding water depth of the location of cross-shore SST minimum (LCSM) averaged from 23°N to 25°N (*solid line* for **a** and **c**), and the related cross-shore wind stress (positive eastward, *dashed line* for **a**) and alongshore wind stress (positive northward, *dashed line* for **c**) averaged at the 8 wind control points from 23°N to 25°N (Fig. 1a, black asterisks) in 2008. Correlation coefficient between the depth of LCSM and cross-shore wind stress (**b**) and alongshore wind stress (**d**) in different lag day conditions

10^{-2} m^2 s^{-1}, with an almost constant value of 3.5×10^{-3} m^2 s^{-1} within the bottom 7 m (Souza et al. 2004). The corresponding depth of the maximum upwelling intensity is expected to occur within the 12.1–38.2 m isobaths. The results of the idealized experiments and the analysis above explain the observation that the LCSM extends along the 25 m isobath north of 23°N, and the onshore wind drives the LCSM to stretch along the 35 m isobath south of 23°N. As a special case, on a shallow shelf like that of Southern Morocco, we see that if the thickness of the Ekman layer is greater than the depth of the outer shelf, a shelf break upwelling cell along with a weak, broad coastal cell may be observed (Estrade et al. 2008). The LCSM may consequently occur over the shelf break.

4 Conclusions

The cross-shore maximum upwelling intensity along the Northwest Africa coast is studied using MODIS SST data from 2008. Using an analytical model, Estrade et al. (2008) inferred that 90 % of the bottom Ekman transport upwells in the region $0.5D < h < 1.25D$, preferentially upwells near the isobath $h \approx 0.6D$, and upwelling shuts down over the inner shelf ($h < 0.4D$). We further use remotely sensed data to verify that the cold water preferentially outcrops at a certain depth, and discuss the factors influencing the LCSM. The result shows that the LCSM stretches along the 25 m isobath north of 23°N and along the 35 m isobath south of 23°N in June 2008. To explain this phenomenon,

we use a two-dimensional analytical model with a constant bottom slope and a smoothed topography in a sample cross-shore section. Furthermore, we find that the depth of LCSM is proportional to both $\sqrt{A_z}$ and $1/\sqrt{f}$. The onshore wind drives the core of upwelling offshore and a weak downwelling near-shore, whereas the offshore wind produces the opposite effect. This effect is verified by a close correlation ($r = -0.65$ with 1 lag day) between the depth of LCSM and cross-shore wind stress using 8-day averaged remotely sensed data from 2008. The alongshore wind acts upon the eddy viscosity and then affects the LCSM ($r = 0.46$ with 1 lag day). Therefore, in a water column with a large eddy viscosity located in a low latitude coastal region, the onshore wind drives the upwelling core to move further offshore. The study of the shift of LCSM, which plays a pivotal role in nutrient transport and aquatics distribution, would provide additional information for commercial fishing.

Acknowledgments This study was originally inspired by the work of Estrade et al. (2008). This research was supported by the Natural Science Foundation of China (grant no. 41076001) and the Fundamental Research Funds for the Central Universities (grant no. 2010121029) of China. We also thank Federico Ienna for editorial assistance with our English, and the two anonymous reviewers for helpful comments on the manuscript.

Appendix: Derivation of the horizontal velocity

Welander (1957) extended the Ekman theory to varying bathymetry. Kamenkovich (1977) added a geostrophic component into the equation associated with the pressure gradient term. Estrade et al. (2008) finally obtained the geostrophic velocity and solved the exact solution using the assumption that cross-shore Ekman transport equals zero. Jiang et al. (2010) used a one-dimensional numerical model to solve the momentum equation. Following their work, in a steady, unstratified, and homogeneous ocean, we assume a constant density $\rho = 1025\ \mathrm{kg\ m^{-3}}$ and vertical eddy viscosity A_z, and ignore the horizontal advection terms. The momentum equation is

$$f\vec{k} \times \vec{V} = -\frac{\nabla P}{\rho} + A_z \frac{\partial^2 \vec{V}}{\partial z^2}, \tag{2}$$

where P is the pressure, f is the Coriolis parameter, and $\vec{k}$ is a vertical unit vector. The solution of the equation can be obtained by separating the horizontal velocity components into an Ekman part and a geostrophic part $\vec{V} = \vec{u}_e + \vec{u}_g$, and by introducing the complex variables $\vec{u}_e = u_e + iv_e$, $\vec{u}_g = u_g + iv_g$, and wind stress $\vec{\tau} = \tau_x + i\tau_y$. Equation (2) can thus be written as

$$\begin{aligned} f\vec{k} \times \vec{u}_e &= A_z \frac{\partial^2 \vec{u}_e}{\partial z^2} \\ f\vec{k} \times \vec{u}_g &= -\frac{\nabla P}{\rho}. \end{aligned} \tag{3}$$

Here, we take a right-handed coordinate system, in which x is in cross-shore direction, positive eastward; positive y is 90° counterclockwise from the positive x-direction; and z is the vertical direction, positive upward. The surface and bottom boundary conditions are

$$\begin{aligned} &z = 0 : \rho A_z \frac{\partial \vec{u}_e}{\partial z} = \vec{\tau} \\ &z = -h : \vec{u}_g + \vec{u}_e = 0. \end{aligned} \tag{4}$$

The solution of Eq. (3) with boundary condition (4) is

$$\vec{u}_e = \frac{\vec{\tau}}{\rho A_z j} \frac{\sinh[j(h+z)]}{\cosh[jh]} - \vec{u}_g \frac{\cosh[jz]}{\cosh[jh]}, \tag{5}$$

in which $j = (1+i)\sqrt{f/2A_z}$. The depth-integrated transport from $z = -h$ to the surface is

$$\begin{aligned} M &= \int_{-h}^{0} \vec{V} \mathrm{d}z \\ &= \frac{\vec{\tau}}{\rho A_z j^2} \left(1 - \frac{1}{\cosh[jh]}\right) + \vec{u}_g \left(h - \frac{1}{j}\tanh[jh]\right). \end{aligned} \tag{6}$$

As Brink (1983) and Mitchum and Clarke (1986) did in their previous studies, we introduce Ekman layer structure functions which simplify the form of the solutions and therefore allow for an intuitive explanation of the results. These functions are defined as

$$\begin{aligned} \delta &= \left\{\cos\left(\frac{h}{D}\right)\cosh\left[\frac{h}{D}\right]\right\}^2 + \left\{\sin\left(\frac{h}{D}\right)\sinh\left[\frac{h}{D}\right]\right\}^2 \\ S_1 &= \frac{1}{\delta}\cos\left(\frac{h}{D}\right)\cosh\left[\frac{h}{D}\right] \\ S_2 &= \frac{1}{\delta}\sin\left(\frac{h}{D}\right)\sinh\left[\frac{h}{D}\right] \\ T_1 &= \frac{1}{\delta}\sinh\left[\frac{h}{D}\right]\cosh\left[\frac{h}{D}\right] \\ T_2 &= \frac{1}{\delta}\sin\left(\frac{h}{D}\right)\cos\left(\frac{h}{D}\right), \end{aligned} \tag{7}$$

where $D = \sqrt{2A_z/f}$ is the Ekman depth. Assuming that wind forcing is uniform and alongshore variation of terrain is small, the $\partial P/\partial y$ term becomes negligible so that the cross-shore geostrophic velocity u_g is zero. We then have the cross-shore Ekman transport

$$M_x = \frac{\tau_y}{\rho f}(1 - S_1) + \frac{\tau_x}{\rho f} S_2 - \frac{v_g D}{2}(T_1 - T_2). \tag{8}$$

The no-flow penetration condition at the shore requires that the cross-shore transport M_x is equal to zero at the coast and must be equal to zero in the entire water column. The geostrophic velocity becomes

$$\vec{u}_g = iv_g = \frac{2i}{\rho f D}\left[\frac{\tau_y(1-S_1)}{T_1-T_2} + \frac{\tau_x S_2}{T_1-T_2}\right]. \quad (9)$$

Substituting expression (9) into Eq. (5), we obtain the horizontal velocity $\vec{V}$ as

$$\vec{V} = \vec{u}_e + \vec{u}_g = \frac{\tau_x + i\tau_y}{\rho A_z j}\frac{\sinh[j(h+z)]}{\cosh[jh]} + \frac{2i}{\rho f D}\left[\frac{\tau_y(1-S_1)}{T_1-T_2} + \frac{\tau_x S_2}{T_1-T_2}\right]\left(1 - \frac{\cosh[jz]}{\cosh[jh]}\right). \quad (10)$$

References

Arístegui J, Barton ED, Álvarez-Salgado XA, Santos AMP, Figueiras FG, Kifani S, Hernández-León S, Mason E, Machú E (2009) Sub-regional ecosystem variability in the Canary Current upwelling. Prog Oceanogr 83:33–48

Brink KH (1983) Low-frequency free wave and wind-driven motions over a submarine bank. J Phys Oceanogr 13:103–116

Estrade P, Marchesiello P, Verdière ACD, Roy C (2008) Cross-shelf structure of coastal upwelling: a two-dimensional extension of Ekman's theory and a mechanism for inner shelf upwelling shut down. J Mar Res 66:589–616

Jiang L, Breaker LC, Yan XH (2010) A model for estimating cross-shore surface transport with application to the New Jersey Shelf. J Geophys Res 115:C04017. doi:10.1029/2009JC005998

Johnson J, Stevens L (2000) A fine resolution model of the eastern North Atlantic between the Azores, the Canary Islands and the Gibraltar Strait. Deep Sea Res I 47:875–899

Kamenkovich VM (1977) Fundamentals of ocean dynamics (trans: Radok R). Elsevier Scientific, New York, pp 127–134

Lentz SJ (1995) Sensitivity of the inner-shelf circulation to the form of the eddy viscosity profile. J Phys Oceanogr 25:19–28

Marcello J, Hernández-Guerra A, Eugenio F, Fonte A (2011) Seasonal and temporal study of the northwest African upwelling system. Int J Remote Sens 32:1843–1859

Mitchum GT, Clarke AJ (1986) The frictional nearshore response to forcing by synoptic scale winds. J Phys Oceanogr 16:934–946

Roy C (1998) An upwelling-induced retention area off Senegal: a mechanism to link upwelling and retention processes. S Afr J Mar Sci 19:89–98

Ryan JP, Yoder JA, Townsend DW (2001) Influence of a Gulf Stream warm-core ring on water mass and chlorophyll distributions along the southern bank of Georges Bank. Deep Sea Res II 48:159–178

Santos AMP, Kazmin AS, Peliz A (2005) Decadal changes in the Canary upwelling system as revealed by satellite observations: their impact on productivity. J Mar Res 63:359–379

Souza AJ, Alvarez LG, Dickey TD (2004) Tidally induced turbulence and suspended sediment. Geophys Res Lett 31:L20309. doi:10.1029/2004GL021186

Welander P (1957) Wind action in a shallow sea: some generalizations of Ekman's theory. Tellus 9:45–52

Wooster WS, Bakum A, McLain DR (1976) The seasonal upwelling cycle along the eastern boundary of the North Atlantic. J Mar Res 34:131–141